Heliyon 10 (2024) e34921

Contents lists available at ScienceDirect

Heliyon

journal homepage: www.cell.com/heliyon

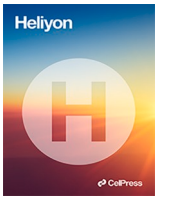

Research article

Fabrication of Ag-doped BiOF-reduced graphene oxide composites for photocatalytic elimination of organic dyes

Md. Elias, Rowshon Alam, Sebak Sarker, Mohammad Awlad Hossain *

Department of Chemistry, Jagannath University, Dhaka-1100, Dhaka, Bangladesh

ARTICLE INFO

Keywords:
Semiconductor
BiOF
Silver
Reduced graphene oxide
Photocatalyst
Photodegradation

ABSTRACT

Bismuth oxyfluoride (BiOF) is an emerging class of material with notable chemical stability, unique layered structure and striking energy band structure. Bi-based semiconductor materials and reduced graphene oxides (rGOs) have attracted considerable attention due to their broad spectrum of potential applications. Herein, we successfully synthesised an efficient photocatalyst comprising BiOF–rGO nanocomposites with embedded Ag nanoparticles using a simple hydrothermal method. The synthesised nanocomposites were characterised through Fourier-transform infrared spectroscopy, X-ray diffraction (XRD), field emission scanning electron microscopy and ultraviolet (UV)–visible spectroscopy. The XRD results indicated the crystalline structures of the BiOF, Ag-doped BiOF and Ag-doped BiOF–rGO composites. Photocatalytic activity assessments focused on the degradation of methylene blue (MB) and methyl orange (MO) dyes under UV-light and sunlight irradiation. The Ag-doped BiOF–rGO composite exhibited significantly enhanced degradation efficiency, achieving 61.81 % and 74.25 % degradation of MB and MO, respectively, after 300 min under UV-light irradiation. On the contrary, pure BiOF demonstrated only 17.63 % and 48.29 % degradation for MB and MO, respectively, under similar conditions. Furthermore, under sunlight irradiation, the Ag-doped BiOF–rGO composite exhibited an MB removal efficiency of 43.87 % after 300 min, whereas pure BiOF showed only 27.47 % under identical conditions. These results underscore the potential of Ag-doped BiOF–rGO composites as highly efficient and adaptable photocatalysts for the photodegradation of organic dyes in industrial wastewater.

1. Introduction

Environmental challenges such as pollution and global energy demand have been the most pressing concerns for humans [1]. Environmental contamination arises from the cumulative impacts of certain human actions over time. This has created a looming problem, jeopardising all forms of life on Earth. Increasing water contamination is one of the most serious issues due to rapid industrialisation and population growth and is a leading cause of fatalities and diseases globally [2]. A large quantity of hazardous organic and inorganic substances has accumulated in water bodies, posing a significant threat to human health [3]. In general, inorganic contaminants comprise cadmium, arsenic, chromium, fluoride, lead, mercury, etc., while organic contaminants include acrylamide, phenol, carbon tetrachloride, benzene hexachloride and various organic dyes such as Congo red, methylene blue (MB) and methyl orange (MO) [4]. Among these pollutants, organic dyes are toxic, mutagenic and carcinogenic, cause chromosomal fractures

* Corresponding author.
E-mail address: awlad1975@yahoo.com (M.A. Hossain).

https://doi.org/10.1016/j.heliyon.2024.e34921
Received 14 March 2024; Received in revised form 12 July 2024; Accepted 18 July 2024
Available online 25 July 2024

and respiratory disorders [4] and are primarily discharged from textile industries.

To remove these organic dyes from wastewater effluents, several processes such as separation, precipitation, solvent extraction, nanofiltration, adsorption and photocatalysis have been employed [5]. The photocatalytic degradation process emerges as the optimal choice for water filtration because it prevents secondary pollution along with the complete mineralisation of organic dyes [6–9]. With the integration of a photocatalyst and photons of light, highly reactive species such as hydroxyl radicals ($^{\bullet}OH$) and superoxide radicals ($^{\bullet}O_2^-$) are formed during photocatalysis [10]. This process occurs when light of proper frequency and energy ($h\upsilon > Eg$, where Eg is the energy gap between the valence band (VB) and conductive band (CB)) falls on the semiconductor and electrons are excited from the VB to the CB, leading to the formation of electron–hole pairs in the semiconductor [10]. Until now, titanium dioxide (TiO_2) has been the most extensively studied semiconductor-based photocatalyst. However, it can only utilise less than 5 % of the total solar energy impinging on the Earth's surface due to its wide band gap (3–3.2 eV) [11]. Various methods have been employed to enhance the light absorption of photocatalysts in the visible (vis) spectral region, including modifications of both TiO_2 and non-TiO_2 semiconductors [11].

Bismuth (Bi)-based semiconductors have attracted research interest owing to their unique photocatalytic properties and applications [12–14]. Bi-based compounds possessed hybridised band structures involving the lone-pair electrons of Bi^{3+} [15]. Hybridised states not only decrease the effective masses of holes and electrons but also facilitate a longer travelling distance for excited carriers [16], effectively reducing the band gaps and enhancing light absorption in the lower-energy region, thereby improving photocatalytic activities [17]. Despite their different crystalline structures, Bi-based photocatalysts exhibited improved photocatalytic activity. These include perovskite, scheelite, pyrochlore, Aurivillius and Sillen structures corresponding to $NaBiO_3$ [18], $BiVO_4$ [19], Bi_2MNbO_7 (M = Al, Ga, In, Fe and Sm) [20], Bi_2MoO_6 [21] and Bi oxyhalide (BiOX) (X = Cl, Br and I) [22], respectively. Among them, the Sillen structure compounds BiOX (X = Cl, Br and I) exhibit more excellent photo-oxidation activity and interesting structure-related properties due to the existence of an active $(Bi_2O_2)^{2+}$ layer [17]. To investigate the structural effects of BiOX compounds, Sijia Zou et al. [15] reported that layered BiOFs have an internal electric field (IEF) perpendicular to the $[Bi_2O_2]^{2+}$ and fluorine anionic slabs, thereby favouring the efficient separation of photogenerated electrons and holes. The synergetic effect of surface structure and bulk IEF significantly improves the activity of Bi oxyfluoride (BiOF) nanosheets. They found that 79.3 % of rhodamine B (RhB) dye is degraded by BiOF after 60 min of ultraviolet (UV) light irradiation, while only 33.7 % of RhB is degraded by commercial rutile TiO_2. These results indicate that a rational modification is required to enhance the photocatalytic activity of BiOF. Doping is one of the most extensively used methods for increasing the photocatalytic activities of metal oxide semiconductors [23]. It has been concluded that semiconductor doping significantly and effectively influences the optical and charge dynamics characteristics, as well as the band structures of semiconductors, and has garnered considerable attention. Recently, Ag has attracted considerable interest as a promising dopant for semiconducting metal oxides owing to its unique features and applications [24]. The influences of Ag metal loading on the crystal structure, morphology, surface chemical state and photocatalytic efficiency of BiOF nanoparticles (NPs) were investigated using X-ray diffraction (XRD) and scanning electron microscopy (SEM) for the photodegradation of organic pollutants (MB and MO). Conversely, reduced graphene oxide (rGO) exhibits remarkable advantageous properties such as superior chemical stability, strong adsorption ability and excellent electronic and conductive properties [14,25]. Additionally, the large electron storage capacity of rGO improves the photocatalytic efficiency by accepting photogenerated electrons from the conduction band of metal oxides at the heterojunction interface of metal oxides and rGO [26]. Therefore, the formation of rGO is usually chosen in the synthesis of photocatalyst materials [24,27–31].

Herein, an Ag-doped BiOF–rGO composite is fabricated using a one-step hydrothermal method. To the best of our knowledge, this is the first report on the use of a hydrothermal method to prepare an Ag-doped BiOF–rGO nanocomposite photocatalyst. The photocatalytic performances of the synthesised composites are investigated using MB and MO dyes under UV-light and sunlight irradiation. This study aimed to establish a relationship between Ag-doped BiOF and rGO and their photocatalytic activities by comparing their crystal structures, morphologies, optical properties, specific surface area and electron–hole separation effects.

2. Experimental section

2.1. Materials

All chemicals and reagents were of analytical grade and were used without further purification. Bi nitrate pentahydrate [$Bi(NO_3)_3{\cdot}5H_2O$], silver nitrate ($AgNO_3$) and ammonium fluoride (NH_4F) were procured from Nova Chemicals, India and used as Bi, Ag, and F sources, respectively. Sulphuric acid (H_2SO_4), MB and MO were purchased from Nova Chemicals, India. Sodium hydroxide (NaOH), potassium permanganate ($KMnO_4$) and sodium nitrate ($NaNO_3$) were procured from Merck, India. Graphite powder, hydrogen peroxide (H_2O_2) and ethanol (CH_3CH_2OH) were purchased from Sigma Aldrich. Moreover, deionised water and distilled water were used in all experimental works.

2.2. Sample preparation

2.2.1. Preparation of Ag-doped BiOF–rGO composites

The Ag-doped BiOF–rGO composite was synthesised via the in situ hydrothermal method. Initially, GO was prepared from graphite powder using the modified Hummers' method, as described in our previous report [5]. The as-prepared GO was used to prepare the Ag-doped BiOF–rGO nanocomposite. To obtain a homogeneous suspension of exfoliated GO (A), 0.1g of the prepared sample was dispersed in ethanol (10 mL) under ultrasonication for 1 h. To prepare the Ag-doped BiOF–rGO nanocomposite photocatalyst, a

solution (B) of Bi nitrate pentahydrate (0.4951 g) and silver nitrate (5 wt%) was prepared by dissolving them in 15 mL of ethylene glycol (EG) in a 50 mL beaker and stirred at 300 rpm. In another beaker, NH_4F solution (C) was prepared by adding 0.3037 g of NH_4F to 5 mL of EG under vigorous stirring. Afterwards, GO suspension A, solution B and solution C were mixed for 1 h of sonication (Powersonic 405, Hwashin Technology Co., Korea) to achieve homogeneous dispersion. The reaction mixture was then decanted into a Teflon-lined stainless steel autoclave and kept for 16 h at 180 °C. Finally, the resultant precipitate of Ag-doped BiOF–rGO was washed and dried at 70 °C in a vacuum oven for 5 h. For comparison, a pure BiOF photocatalyst was prepared by dissolving Bi nitrate pentahydrate and ammonium fluoride in EG solution. A schematic flow diagram of the preparation of the Ag-doped BiOF–rGO nanocomposite photocatalyst by the hydrothermal method is presented in Fig. 1.

2.3. Characterisation of prepared samples

The morphological characterisation of the photocatalysts was conducted by field emission SEM (FE-SEM, JSM-7600F, JEOL, Japan) at an accelerating voltage of 10 kV. Fourier transform infrared (FTIR) analysis was performed using an IR-Prestige-21 spectrophotometer (Shimadzu Corp., Japan) using KBr as a standard to determine the presence of various functional groups and the formation of samples. Optical absorption spectra were obtained using UV–vis spectroscopy (UV-1800, Shimadzu, Japan) at a wavelength range of 200–800 nm. XRD analysis was performed using a Shimadzu XRD-6000 diffractometer equipped with Cu-Kα radiation with a wavelength (λ) of 1.54056 Å. The analysis was conducted at 40 kV with a scan rate of 0.02° over the 2θ range of 10°–90° at 25 °C. This provided valuable insights into the confirmation of crystal structures. The Scherrer formula was applied to the most intense diffraction peak to calculate the average crystalline size.

2.4. Photocatalytic activity tests

The photocatalytic performances of the prepared samples were evaluated by degrading MB and MO dyes under UV-light and sunlight irradiation. Controlled experiments were conducted using a rectangular aluminium foil-supported wooden reactor equipped with a 60 W low-pressure mercury lamp (λ = 254 nm, irradiance = 30 mW/cm^2) as the UV-light source and a 200 W tungsten lamp (2150 lm with a wavelength range of 500–620 nm) as the vis-light source. In this experiment, 50 mg of the photocatalyst was dispersed in 100 mL of a 10 ppm aqueous solution of dye (MB or MO) at room temperature under continuous stirring. The solution was stirred in the dark for 1 h to achieve adsorption–desorption equilibrium between the photocatalysts and dye.

In the degradation studies, approximately 3 mL of the aliquot solution was collected at regular intervals (every 30 min) and then centrifuged. The supernatant solution was then investigated by UV–vis spectroscopy (UV-1800, Shimadzu, Japan). The maximum absorption peaks of the MB and MO solutions were observed at 664 and 464 nm, respectively. The photodegradation efficiency (%) of

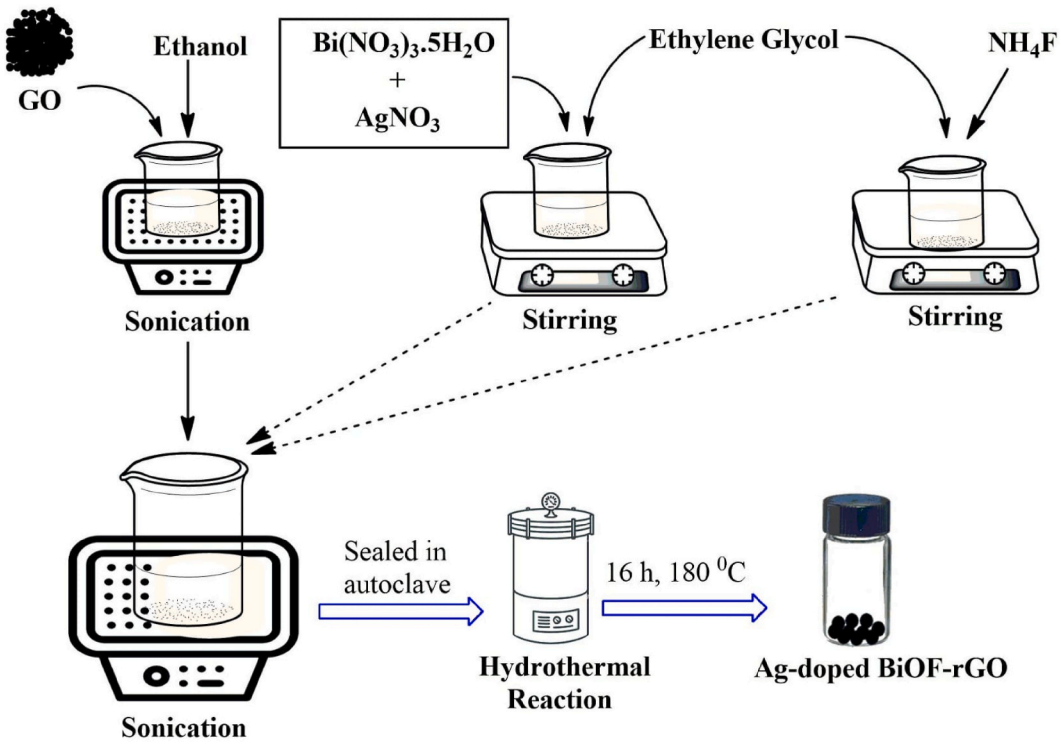

Fig. 1. Schematic flow diagram of the preparation of the Ag-doped BiOF–rGO nanocomposite photocatalyst using the hydrothermal method.

the dyes (MB/MO) was calculated as follows [5].

$$\textbf{Efficiency}\ (\%) = (C_0 - C_t) / C_0 \times 100 \approx (A_o - A_t) / A_o \times 100 \quad (1)$$

where A_0 is the absorbance of the dyes (MB/MO) before treatment and A_t is the absorbance after treatment at time t.

3. Results and discussion

3.1. XRD analysis

The phase structure and crystallinity of the prepared samples were analysed by XRD. Fig. 2 shows the XRD patterns of pure BiOF, Ag-doped BiOF and Ag-doped BiOF–rGO composites. All composites show some common characteristic peaks, although several peaks have very low intensity for pure BiOF, located at 2θ values of 27.78°, 28.84°, 29.24°, 30.87°, 33.78°, 38.26°, 39.39°, 43.88°, 44.8°, 48.72°, 50.56°, 56.66°, 62.69°, 64.65°, 70.33°, 72.35° and 77.660°, corresponding to the (101), (002), (401), (20-3), (110), (102), (004), (003), (112), (200), (201), (211), (212), (104), (114), (213) and (301) planes of the zavaritskite-type tetragonal phase of BiOF (JCPDS no. 01-086-1648; space group: P4/nmm:2), respectively, which agrees well with previous reports [15,32]. No peaks related to the fcc Ag crystal are observed for Ag-doped BiOF, indicating that Ag ions successfully substituted into the zavaritskite BiOF lattice [33, 43]. For Ag-doped BiOF, no characteristic peaks of Ag are observed, but an additional peak at 23.50, marked by '*', characteristic of the rGO (002) crystalline plane of the hexagonal structure is obtained [34–36], confirming that GO was completely reduced to rGO. In addition, to identify the crystalline phase, XRD data were used to estimate the average crystallite size, D, calculated from the peak half-width β, using the Scherrer equation [25].

$$D = \frac{k\lambda}{\beta \cos\theta} \quad (2)$$

where k is the shape factor of the particle and λ and θ are the wavelength and incident angle of the X-rays, respectively. Based on the Scherrer equation, the average crystal sizes of pure BiOF, Ag-doped BiOF and Ag-doped BiOF–rGO composites are 31.89, 43.91 and 14.65 nm, respectively.

3.2. FTIR analysis

The FTIR spectrum is characteristic of a particular compound, providing information about its functional groups, molecular geometry and inter/intramolecular interactions. Fig. 3 depicts the FTIR spectra of the GO, BiOF, Ag-doped BiOF and Ag-doped BiOF–rGO composites. For the BiOF, Ag-doped BiOF and Ag-doped BiOF–rGO composites, the characteristic peaks at 513 and 644 cm^{-1} are attributed to the stretching and asymmetrical stretching vibrations of the Bi–O bond, respectively [10], confirming the presence of BiOF in the composite. This is consistent with the XRD data of the formation of BiOF. Moreover, the broad bands at 3400–3500, 2346 and 1530 cm^{-1} are assigned to the O–H stretching vibrations of adsorbed water molecules on particles, stretching vibration of the C=O bond of atmospheric CO_2 molecules and asymmetric stretching vibration of N–O bonds, respectively [10,37]. For Ag-doped BiOF and Ag-doped BiOF–rGO, no significant peaks were observed for Ag NPs. This absence of peaks can be attributed to the development of organic or inorganic capping through complexations with functional groups [38]. Additionally, in the Ag-doped BiOF–rGO composite shown in Fig. 2, the bands associated with oxygen functionalities [39] were nearly absent in the spectra. This confirms the effective reduction of GO sheets.

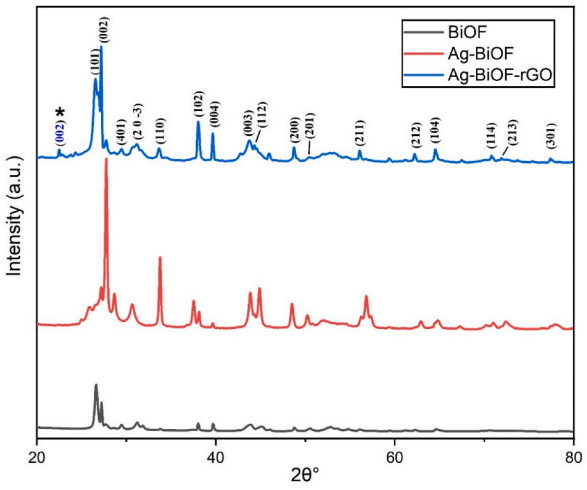

Fig. 2. Combined XRD patterns of pure BiOF, Ag-doped BiOF and Ag-doped BiOF–rGO composites.

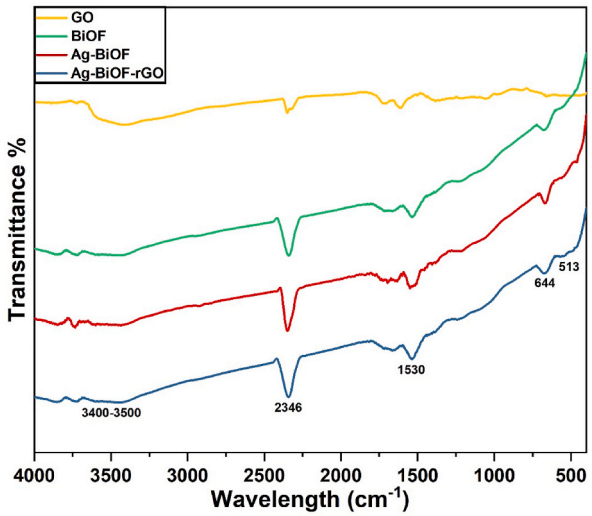

Fig. 3. FTIR spectra of GO, pure BiOF, Ag-doped BiOF and Ag-doped BiOF–rGO composites.

3.3. FE-SEM analysis

The morphologies of the as-prepared samples was analysed using FE-SEM. Here, Fig. 4(a–c) show the FE-SEM micrographs of the BiOF, Ag-doped BiOF and Ag-doped BiOF–rGO catalysts. The image in Fig. 4(a) shows that BiOF mainly comprises aggregated nanoflakes and rod-like nanoplates. As shown in Fig. 4(b), the fabricated Ag-doped BiOF demonstrates spherical shaped Ag NPs congregated on the BiOF surface with few modifications of the morphology of the host BiOF. Spherical shaped Ag NPs for Ag-doped BiOF–rGO catalysts [Fig. 4(c)], as indicated by rectangular boxes, were deposited on the surface of rGO, consistent with previous research [33]. This morphology is characterised by wrinkled, transparent and ultrathin paper-like rGO sheets, similar to those reported previously [40]. Moreover, BiOF exhibits an aggregated morphology in Ag-doped BiOF–rGO, indicating the presence of Ag NPs, as shown in the previous graph [Fig. 4(b)]. To obtain elemental information about the synthesised composites, EDS spectra were collected. Fig. 4(d) depicts the EDS spectrum of the BiOF composite, which reveals the presence of Bi, O and F and confirms that the synthesised composite is indeed BiOF. In addition, Fig. 4(e) and (f) depict the presence of Ag, Bi, O and F in Ag-doped BiOF and Ag, Bi, O, F and C in Ag-doped BiOF–rGO composites, respectively, confirming the successful preparation of Ag-doped BiOF and Ag-doped BiOF–rGO composites. Percentages of the atomic compositions of the synthesised photocatalysts are presented in Table 1.

3.4. UV–vis absorption spectra

The optical performances of synthesised semiconductor materials were characterised through UV–vis absorption spectroscopy. Fig. 5(a) shows the UV–vis absorption spectra of pure BiOF, Ag-doped BiOF and Ag-doped BiOF–rGO nanocomposites dispersed in absolute ethanol. Among all samples, BiOF and Ag-doped BiOF–rGO exhibit almost identical absorption peaks at 222 and 308 nm. For Ag-doped BiOF, the first peak at a lower wavelength is completely similar to that of BiOF. However, the next peak is almost 24 nm less blue-shifted than that of the band gap absorption of bulk BiOF at 308 nm, which might be explained by the quantum confinement effect of the smaller feature size of BiOF [25]. The band gap of the prepared composites was calculated using the Tauc equation [5].

$$\alpha = \frac{K(h\nu - E_g)^n}{h\nu} \tag{3}$$

where α is the optical absorption coefficient, K is a constant, E_g is the band gap, $h\nu$ is the photon energy and n can be 0.5 or 2 depending on the transition, i.e. direct or indirect [41]. BiOF displays a direct band gap [42]. Thus, Equation (3) can be expressed for the direct band gap as follows:

$$(\alpha h\nu) = K(h\nu - E_g)^{0.5} \tag{4}$$

After modification, Equation (4) becomes

$$(\alpha h\nu)^2 = K^2(h\nu - E_g) \tag{5}$$

The optical band gaps of the produced samples were determined by extrapolating the linear portion of the Tauc plot $(\alpha h\nu)^2$ versus $h\nu$, as illustrated in Fig. 5(b). The calculated band gaps of pure BiOF, Ag-doped BiOF and Ag-doped BiOF–rGO composites were calculated to be 4.50, 3.15 and 2.90 eV, respectively. The Ag-doped BiOF–rGO composite exhibited a lower band gap, indicating enhanced photocatalytic activity in both vis and UV regions compared with pure BiOF and Ag-doped BiOF catalysts.

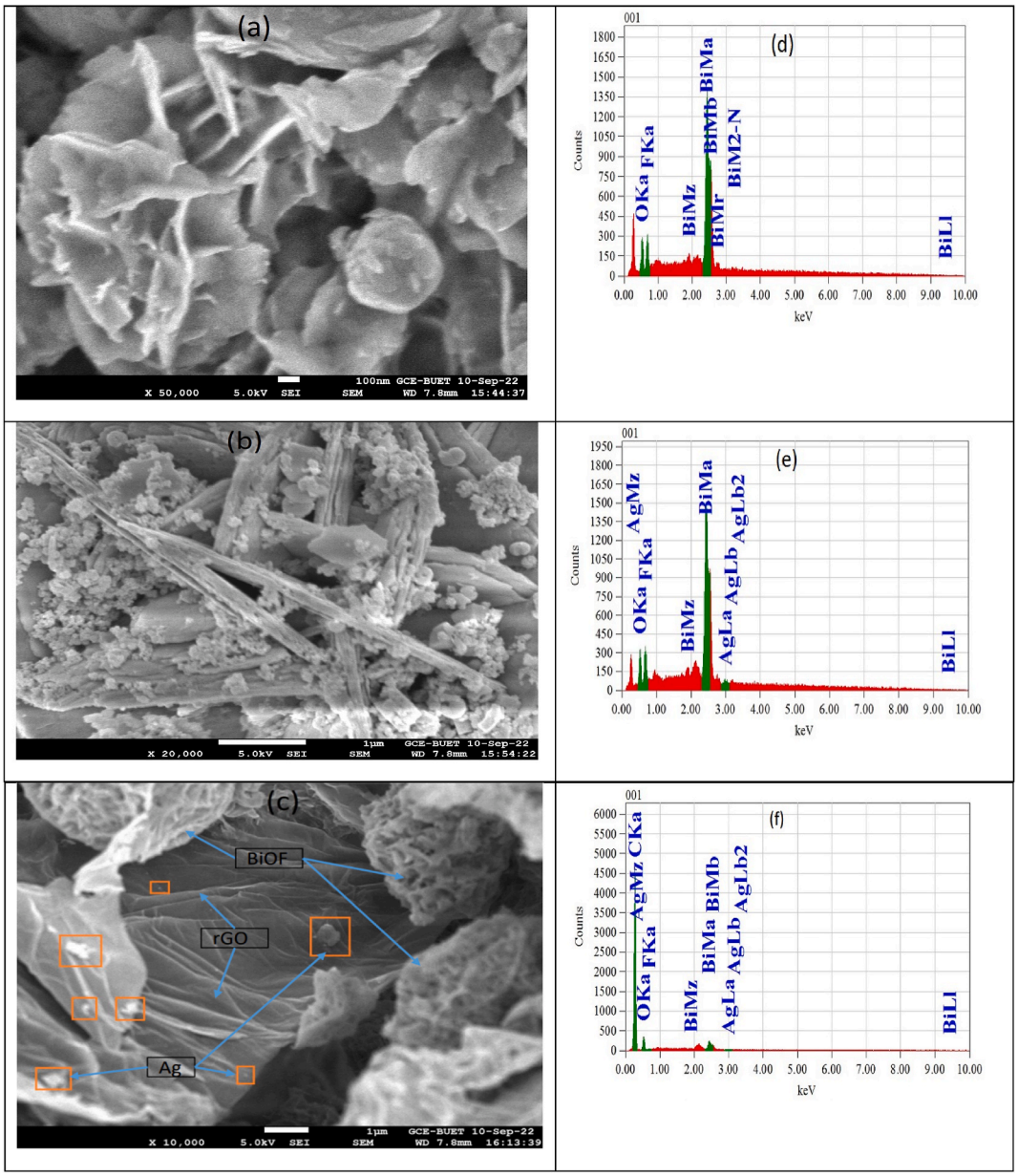

Fig. 4. FE-SEM images of (a) BiOF, (b) Ag-doped BiOF and (c) Ag-doped BiOF–rGO composites; EDS spectra of (d) BiOF, (e) Ag-doped BiOF and (f) Ag-doped BiOF–rGO composites.

Table 1
Elemental analysis of pure BiOF, Ag-doped BiOF and Ag-doped BiOF–rGO nanocomposites.

Samples	M (Bi)		K (O)		K (F)		L* (Ag)		K* (C)	
	wt%	at%	wt%	at%	wt%	at%	wt%	at%	wt%	at%
Pure BiOF	90.81	45.45	3.80	24.83	5.40	29.72				
Ag-doped BiOF	89.50	45.05	3.63	23.88	5.34	29.58	1.53	1.49		
Ag-doped BiOF–rGO	11.73	0.78	9.55	8.30	0.19	0.14	0.13	0.02	78.38	90.76

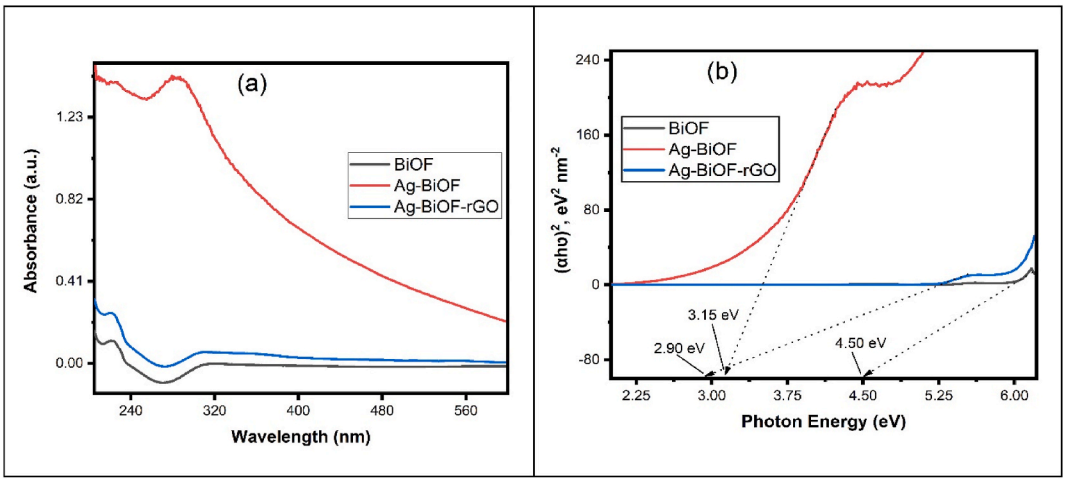

Fig. 5. (a) UV–vis absorption spectra of pure BiOF, Ag-doped BiOF and Ag-doped BiOF–rGO composites; (b) calculated band gaps from Tauc plots of pure BiOF, Ag-doped BiOF and Ag-doped BiOF–rGO photocatalysts.

3.5. Photocatalytic activity assessment

To determine the photocatalytic activities of pure BiOF, Ag-doped BiOF and Ag-doped BiOF–rGO composites under UV-light and sunlight irradiation. Both MB and MO were selected as model pollutants. The details are discussed in the following sections.

3.5.1. Degradation of the MB dye under UV light

Fig. 6(a) shows the photodegradation efficiency of the MB dye under UV-light irradiation of the BiOF, Ag-doped BiOF and Ag-doped BiOF–rGO composites. Fig. 6(b) shows the gradual changes in absorbance at the characteristic wavelength of 664 nm for the MB dye in the presence of the Ag-doped BiOF–rGO composite under UV-light irradiation. As shown in Fig. 6(a), after 5 h of UV–vis irradiation, pure BiOF, Ag-doped BiOF and Ag-doped BiOF–rGO exhibited efficiencies of 17.63 %, 21.69 % and 61.81 %, respectively. The blank test confirmed minimal MB degradation, indicating insignificant self-photolysis of MB. These results suggest that the Ag-doped BiOF sample displayed slightly higher photocatalytic activity than pure BiOF in the degradation of MB. However, the introduction of rGO into Ag-doped BiOF improved the photocatalytic activity (61.81 % efficiency) for MB dye degradation. A similar result was also found in a previous study [43], attributed to the introduction of rGO into Y-doped BiOF. In that study, while pure BiOF and Y-doped BiOF showed only 15.25 % and 12.54 % MB dye degradation, respectively, the composite Y–BiOF/rGO exhibited the highest MB degradation. This was attributed to the support provided by rGO, which extended the lifetime of photogenerated electron–hole (e^-/h^+) pairs.

In addition, the photocatalytic activity of the MB dye follows pseudo-first-order reaction kinetics as follows [5].

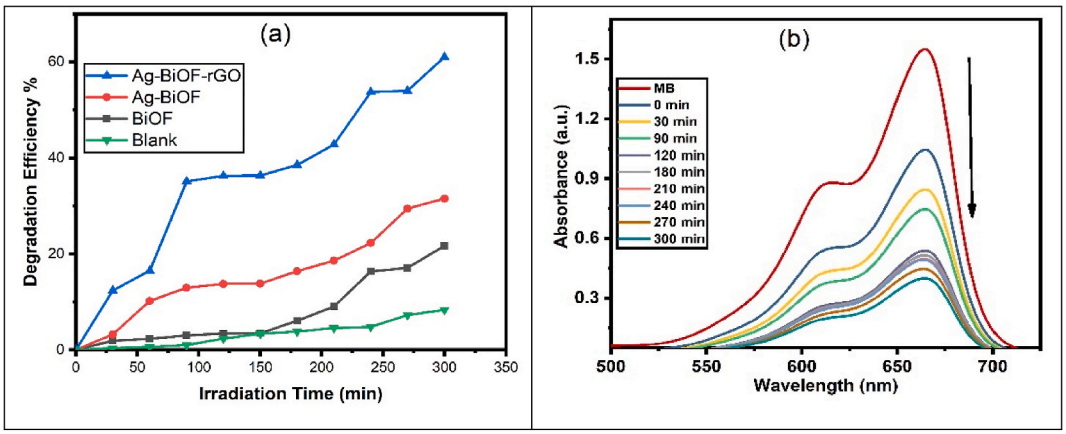

Fig. 6. (a) Photocatalytic activities of pure BiOF, Ag-doped BiOF and Ag-doped BiOF–rGO photocatalysts on methylene blue (MB) under ultraviolet (UV)-light irradiation; (b) UV–visible spectra for degradation of MB with the Ag-doped BiOF–rGO photocatalyst under UV-light irradiation (catalyst dose: 50 mg, dye concentration: 10 ppm, temp.: 25 °C ± 2 °C). (For interpretation of the references to colour in this figure legend, the reader is referred to the Web version of this article.)

$$ln\,(C_t / C_o) = -\,kK_t = -\,k_{app}.t \quad (6)$$

where k_{app} is the apparent pseudo-first-order rate constant (min^{-1}) and C_0 and C_t are the initial and final concentrations of MB at reaction time t, respectively. The values of rate constants (k_{app}) can be found by plotting of $-ln(C_t/C_0)$ as a function of reaction time, as shown in Fig. 7(a). As shown in Fig. 7(b), the rate constant follows the order Ag-doped BiOF–rGO (0.0029 min^{-1}) > Ag-doped BiOF (0.00072 min^{-1}) > BiOF (0.00050 min^{-1}). Ag-doped BiOF–rGO exhibits the best photocatalytic efficiency with a rate constant considerably higher than those of the other photocatalysts under UV-light irradiation for MB dye degradation.

3.5.2. Degradation of the MO dye under UV light

The photocatalytic activities of the synthesised samples were also determined by degrading the MO dye. Fig. 8(a) shows the degradation efficiency of MO with respect to degradation time of all prepared composites, and Fig. 8(b) shows the gradual changes in the absorbance of the MO dye solution in the presence of the Ag-doped BiOF–rGO composite under UV-light irradiation. As shown in Fig. 7(a), pure BiOF, Ag-doped BiOF and Ag-doped BiOF–rGO composites displayed efficiencies of 48.29 %, 49.90 % and 74.25 % after 5 h of UV-light irradiation, respectively. In this case, a blank test was also performed and no significant change in the self-photodegradation of the MO dye was observed. These results confirmed that the Ag-doped BiOF–rGO composite exhibited enhanced photodegradation (74.25 %) compared to pure BiOF and Ag-doped BiOF composite for the degradation of MO dye. Although there have been a few works related to Bi oxyfluoride-based photocatalysts such as Y–BiOF/rGO [43], Ag–BiOF/g-C_3N_4 [32] and BiOCl/BiOF [44] applied for the remediation of contaminants, our synthesised composite Ag-doped BiOF–rGO is entirely novel and efficient for degrading MO and MB dyes (section-3.5.1) compared to pure BiOF and Ag-doped BiOF. The reasons mainly stem from the narrow band gap, smaller particle size and lower recombination rate of the photogenerated electron–hole (e^-/h^+) pairs.

Additionally, Fig. 9(a) shows the plot of $-\ln(Ct/C_0)$ as a function of reaction time to investigate the photodegradation kinetics of the prepared samples with MO dye. According to Fig. 9(b), the rate constant follows the order Ag-doped BiOF–rGO (0.0035 min^{-1}) > Ag-doped BiOF (0.0021 min^{-1}) > BiOF (0.0021 min^{-1}). Therefore, the Ag-doped BiOF–rGO composite exhibits superior photocatalytic efficiency, as characterised by a rate constant that significantly exceeds those of the other photocatalysts, when subjected to UV light for the degradation of MO dye.

3.5.3. Degradation of MB and MO dyes under sunlight

The photocatalytic capabilities of the fabricated samples were further investigated by observing the degradation of MB and MO dyes under sunlight exposure. In this system, the Ag-doped BiOF–rGO nanocomposites also showed better photocatalytic performance (43.87 % degradation efficiency) under sunlight irradiation for 5 h compared to the BiOF photocatalyst, which only showed 27.47 % efficiency under the same conditions for MB degradation [Fig. 10(a)]. Moreover, the Ag-doped BiOF–rGO and BiOF nanocomposites degraded only 17.08 % and 11.50 %, respectively, of MO under the same conditions (sunlight irradiation for 5 h), as depicted in Fig. 10 (b). According to previous work [32], pure BiOF exhibits minimal MB degradation efficiency (12 %) after 6 h of vis-light irradiation, while the efficiency significantly increases after modification of BiOF.

3.5.4. Comparative discussion

The photodegradation efficiency depends on the recombination rate of e^-/h^+ pair generated by UV or vis-light illumination as well as the light absorption ability of the photocatalyst [45]. Based on this statement and the above findings, Ag-doped BiOF–rGO exhibits efficient photocatalytic activity (MO: 74.25 %, MB: 61.81 %) compared to pure BiOF and Ag-doped BiOF composites, which showed only 48.29 % and 49.90 % MO dye degradation and 17.63 % and 21.69 % MB dye degradation, respectively, after 5 h of UV-light irradiation. Moreover, the Ag-doped BiOF–rGO composite exhibited better photocatalytic performance under sunlight irradiation

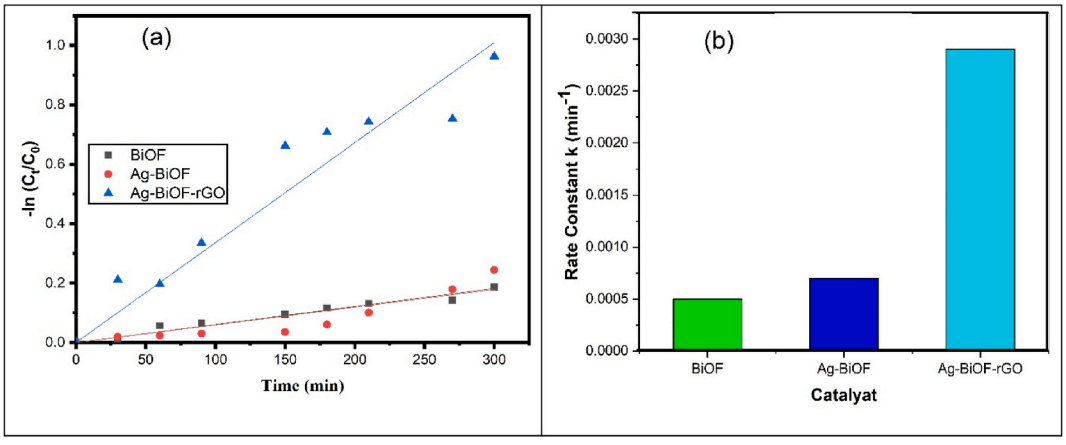

Fig. 7. (a) Pseudo-first-order rate kinetics and (b) reaction rate constants (min^{-1}) for photocatalytic degradation of MB dye using pure BiOF, Ag-doped BiOF and Ag-doped BiOF–rGO nanocomposites (catalyst dose: 50 mg, dye concentration: 10 ppm, temp.: 25 °C ± 2 °C).

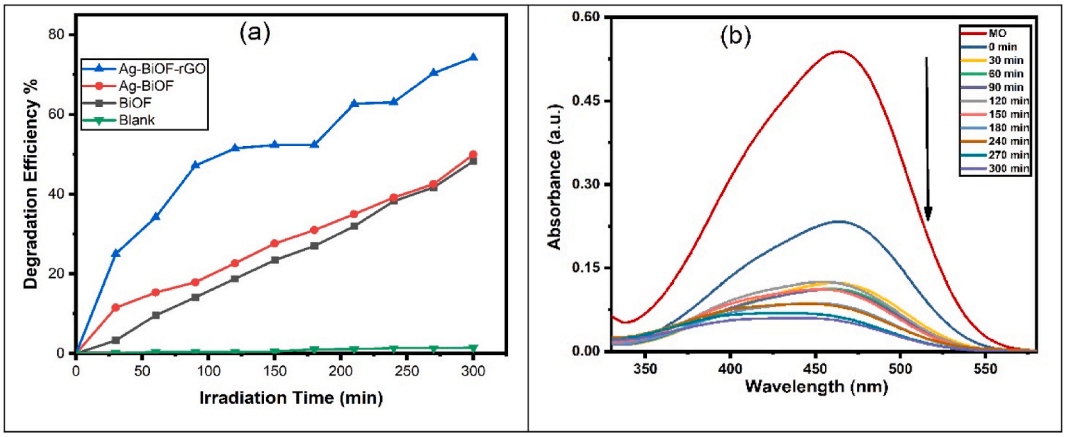

Fig. 8. (a) Photocatalytic activities of pure BiOF, Ag-doped BiOF and Ag-doped BiOF–rGO photocatalysts on MO under UV-light irradiation; (b) UV–visible spectra for degradation of MO with the Ag-doped BiOF–rGO photocatalyst under UV-light irradiation (catalyst dose: 50 mg, dye concentration: 10 ppm, temp.: 25 °C ± 2 °C).

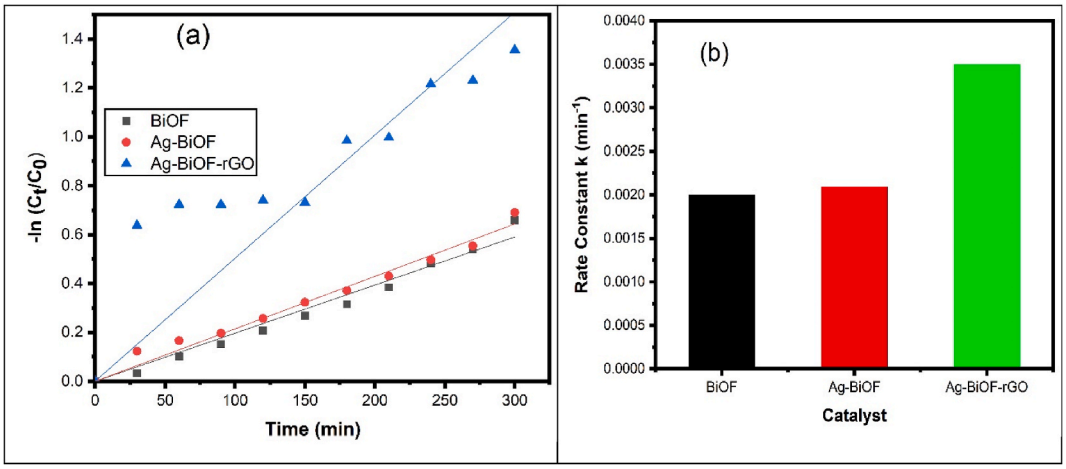

Fig. 9. (a) Pseudo-first-order rate kinetics and (b) reaction rate constants (min^{-1}) for the photocatalytic degradation of MO dye using pure BiOF, Ag-doped BiOF and Ag-doped BiOF–rGO nanocomposites (catalyst dose: 50 mg, dye concentration: 10 ppm, temp.: 25 °C ± 2 °C).

than those of pure BiOF (section 3.5.3). The enhance photocatalytic activity of the Ag-doped BiOF–rGO composites was mainly due to their lower bandgap [5] (section 3.4) and smaller particle size [5] (section 3.1) than those of pure BiOF and Ag-doped BiOF composites. Moreover, the Ag-doped BiOF–rGO composite can transfer a photogenerated electron towards the rGO sheet and reduced the recombination rate of e^-/h^+ pairs [27]. The Ag-doped BiOF–rGO catalyst is positively influenced by the favourable band structure of BiOF and exhibits a layered structure of $[Bi_2O_2]^{2+}$ and fluorine anionic slabs [15]. Between the layers has a perpendicular IEF that is believed to induce effective separation of the photogenerated e^-/h^+ pairs [15], which is also responsible for the improvement of the photocatalytic performance of the Ag-doped BiOF–rGO composite [44]. The photocatalytic efficiencies of the Ag-doped BiOF–rGO composite and previously reported photocatalysts are compared in Table 2.

3.6. Proposed possible degradation mechanism

A plausible mechanistic pathway for the photocatalytic degradation of MB by the Ag-doped BiOF–rGO composite was elucidated based on the above findings and is shown in Fig. 11. The mechanism is described as follows. The Ag-doped BiOF–rGO composite exhibits improved photocatalytic performance because of its synergistic effect, which enhances the effective separation of photogenerated e^-/h^+ pairs. In accordance with related reports, it is hypothesised that rGO contributes to the separation of e^-/h^+ pairs by directing them towards the interface, thereby augmenting the photocatalytic activity of the photocatalysts [14]. Pure BiOF and Ag-doped BiOF exhibit low photocatalytic efficiency owing to the minimal contribution of e^-/h^+ pairs in the photochemical reaction. In contrast, the Ag-doped BiOF–rGO composite mitigates e^-/h^+ pairs recombination by channelling electrons towards the rGO sheet. When the BiOF is exposed to light irradiation, it generates charge carriers (e^-/h^+), with electrons from the VB of the BiOF being excited

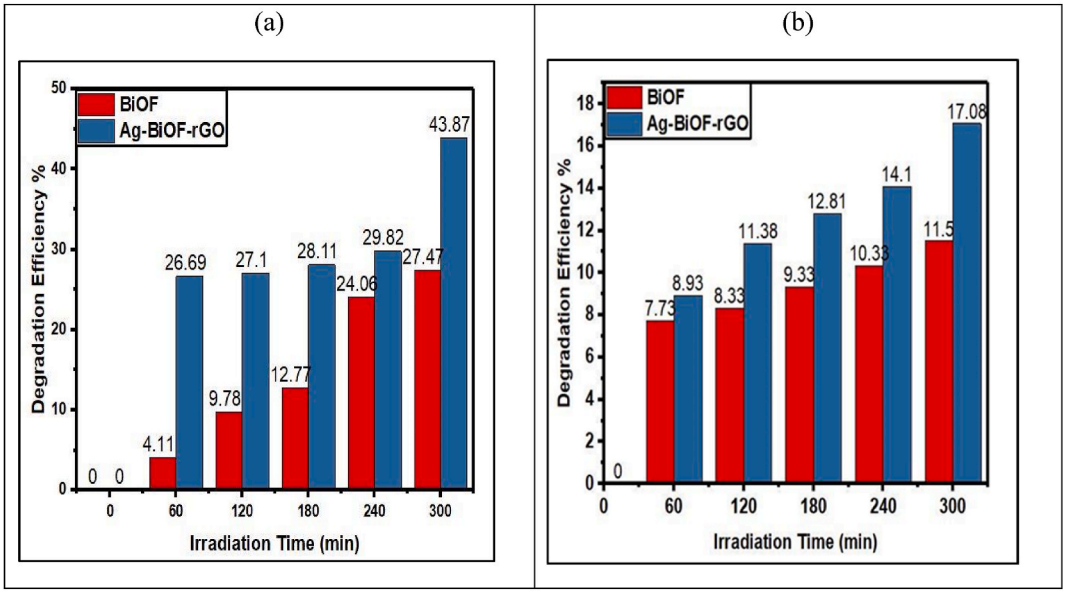

Fig. 10. Photocatalytic activities of pure BiOF and Ag-doped BiOF–rGO photocatalysts on (a) MB and (b) MO under sunlight irradiation (catalyst dose: 50 mg, dye concentration: 10 ppm, temp.: 25 °C ± 2 °C).

Table 2
Comparison of the photocatalytic efficiencies of different photocatalysts for dye degradation.

Catalyst	Model Pollutant	Conc.	Light Source	Time (min)	Degradation (%)	Ref.
BiOBr	MO	10 mg/L	Visible	90	50	[46]
Bi_2InTaO_7	MB	42 mg/L	Visible	170	27.9	[46]
BiOBr	RhB	60 mg/L	UV	30	55	[46]
BiOF/g-C_3N_4	MB	7.5 mg/L	Visible	300	45	[32]
BiOI	MB	40 mg/L	Visible	120	43	[14]
Ag–BiOF–rGO	MB	10 mg/L	UV	300	61.81	This work
Ag–BiOF–rGO	MO	10 mg/L	UV	300	74.25	This work

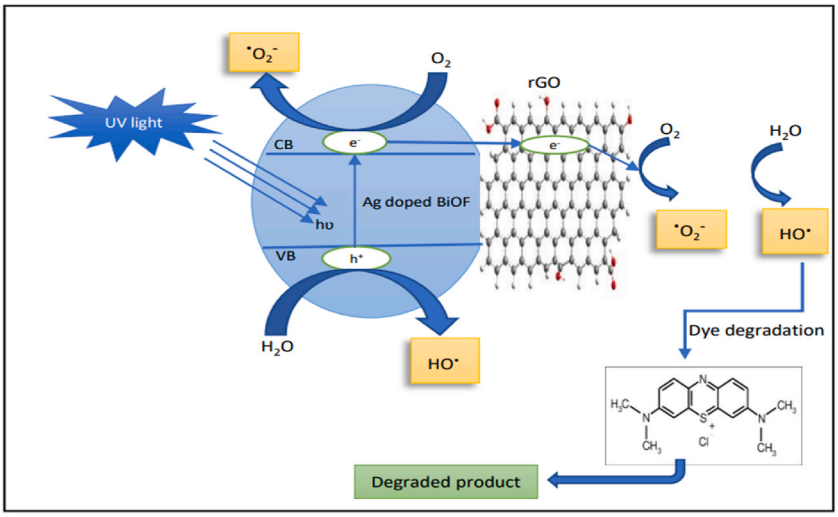

Fig. 11. Schematic of the photodegradation mechanism of the Ag-doped BiOF–rGO catalyst under UV-light irradiation.

to the CB. The presence of Ag^{+} ions in the BiOF lattice enhances the excitation rate. Subsequently, the electrons are transferred to the rGO sheet, extending the lifetime of the photoexcited electron–hole pairs. Concurrently, electrons (e^{-}) in the rGO sheet reduce the molecular oxygen (O_2) to $^{\bullet}O_2^{-}$, leading to the degradation of the dye molecules. Simultaneously, photogenerated holes (h^{+}) in the VB contribute to the production of $^{\bullet}OH$ radicals from water, further facilitating the successful degradation of MB into harmless by-products [47–49]. Additionally, the interfacial defects of photocatalysts enhance the overall photocatalytic activity by trapping electrons when the trap depth is not too deep, which retards the recombination process [50]. In contrast, the co-trapping of both electrons and holes reduces the activity by accelerating the recombination rate of photogenerated e^{-}/h^{+} pairs [51]. However, the photocatalytic mechanism involved the synergistic effect of the Ag-doped BiOF–rGO composites. Therefore, the Ag-doped BiOF–rGO composite exhibits enhanced photocatalytic activity under both UV-light and sunlight irradiation.

4. Conclusions

Herein, the fabrication of BiOF, Ag-doped BiOF and Ag-doped BiOF–rGO composites was successfully achieved using an uncomplicated hydrothermal method. The synthesised composites were characterised by XRD, UV–vis spectrophotometry and FTIR spectroscopy. The FTIR results confirmed the effective conversion of GO to rGO in the Ag-doped BiOF–rGO nanocomposite. These prepared materials were employed for the degradation of industrial pollutants, specifically MB and MO, serving as model dyes under both UV–vis-light and sunlight irradiation. Among all the composites, Ag-doped BiOF–rGO demonstrated superior photocatalytic performance, attributed primarily to its large surface area (resulting in a smaller particle size of only 14.65 nm), a narrow band gap of 2.90 eV and efficient charge separation facilitated by the shifting of electrons towards the rGO sheet, functioning as an electron collector and transporter. Consequently, this process extends the lifetime of charge carriers. These findings emphasise the distinctive quality of the rGO-based Ag–BiOF composite, highlighting its excellent photocatalytic properties, which mitigate the recombination of photogenerated electron–hole pairs. This study unveils new possibilities for developing highly efficient vis-light-driven catalysts suitable for the photodegradation of organic dyes.

Data availability statement

The data described in the present research are accessible from the authors who wrote it upon request.

CRediT authorship contribution statement

Md. Elias: Writing – original draft, Conceptualization, Formal analysis, Investigation. **Rowshon Alam:** Writing-review & editing, Formal analysis, Data curation. **Sebak Sarker:** Methodology, Formal analysis. **Mohammad Awlad Hossain:** Resources, Writing – review & editing, Formal analysis, Conceptualization, Supervision & Investigation.

Declaration of competing interest

The authors declare that they have no known competing financial interests or personal relationships that could have appeared to influence the work reported in this paper.

Acknowledgments

The authors are very much grateful to Jagannath University, Dhaka, Bangladesh for generous financial support to materialize this research work.

References

[1] M. Elias, M. Uddin, J. Saha, A. Hossain, D. Sarker, S. Akter, I. Siddiquey, J. Uddin, A highly efficient and stable photocatalyst; N-doped ZnO/CNT composite thin film synthesized via simple sol-gel drop coating method, Molecules 26 (2021) 1470, https://doi.org/10.3390/molecules26051470.
[2] M. Elias, S. Akter, M.A. Hossain, M.H. Suhag, Fabrication of Zn3(PO4)2/carbon nanotubes nanocomposite thin film via sol-gel drop coating method with enhanced photocatalytic activity, Thin Solid Films 717 (2021) 138472, https://doi.org/10.1016/j.tsf.2020.138472.
[3] V. Koli, S.-C. Ke, A. Dhodamani, S. Deshmukh, J.-S. Kim, Boron-doped TiO2-CNT nanocomposites with improved photocatalytic efficiency toward photodegradation of toluene gas and photo-inactivation of Escherichia coli, Catalysts 10 (2020) 632, https://doi.org/10.3390/catal10060632.
[4] S.K. Sahoo, G. Hota, Chapter 12 - functionalization of graphene oxide with metal oxide nanomaterials: synthesis and applications for the removal of inorganic, toxic, environmental pollutants from water, in: C. Mustansar Hussain (Ed.), Handb. Funct. Nanomater. Ind. Appl., Elsevier, 2020, pp. 299–326, https://doi.org/10.1016/B978-0-12-816787-8.00012-0.
[5] R. Alam, M.A. Hossain, M. Elias, Amine functionalized graphene oxide decorated with ZnO-WO3 nanocomposites for remediation of organic dye from wastewater, J. Phys. Chem. Solid. 190 (2024) 112015, https://doi.org/10.1016/j.jpcs.2024.112015.
[6] G. Williams, B. Seger, P. V Kamat, TiO2-Graphene nanocomposites. UV-assisted photocatalytic reduction of graphene oxide, ACS Nano 2 (2008) 1487–1491, https://doi.org/10.1021/nn800251f.
[7] B. Priya, P. Raizada, N. Singh, P. Thakur, P. Singh, Adsorptional photocatalytic mineralization of oxytetracycline and ampicillin antibiotics using Bi2O3/BiOCl supported on graphene sand composite and chitosan, J. Colloid Interface Sci. 479 (2016) 271–283, https://doi.org/10.1016/j.jcis.2016.06.067.
[8] K. Sharma, V. Dutta, S. Sharma, P. Raizada, A. Hosseini-Bandegharaei, P. Thakur, P. Singh, Recent advances in enhanced photocatalytic activity of bismuth oxyhalides for efficient photocatalysis of organic pollutants in water: a review, J. Ind. Eng. Chem. 78 (2019) 1–20, https://doi.org/10.1016/j.jiec.2019.06.022.
[9] M. Elias, M.K. Amin, S.H. Firoz, M.A. Hossain, S. Akter, M.A. Hossain, M.N. Uddin, I.A. Siddiquey, Microwave-assisted synthesis of Ce-doped ZnO/CNT composite with enhanced photo-catalytic activity, Ceram. Int. 43 (2017) 84–91, https://doi.org/10.1016/j.ceramint.2016.09.114.

[10] M. Elias, M.N. Uddin, M.A. Hossain, J.K. Saha, I.A. Siddiquey, D.R. Sarker, Z.R. Diba, J. Uddin, M.H. Rashid Choudhury, S.H. Firoz, An experimental and theoretical study of the effect of Ce doping in ZnO/CNT composite thin film with enhanced visible light photo-catalysis, Int. J. Hydrogen Energy 44 (2019) 20068–20078, https://doi.org/10.1016/j.ijhydene.2019.06.056.

[11] D.R. Sarker, M.N. Uddin, M. Elias, Z. Rahman, R.K. Paul, I.A. Siddiquey, M.A. Hasnat, M.R. Karim, M.A. Arafath, J. Uddin, P-doped TiO_2-MWCNTs nanocomposite thin films with enhanced photocatalytic activity under visible light exposure, Clean. Eng. Technol. 6 (2022) 100364, https://doi.org/10.1016/j.clet.2021.100364.

[12] V. Dutta Sonu, S. Sharma, P. Raizada, A. Hosseini-Bandegharaei, V. Kumar Gupta, P. Singh, Review on augmentation in photocatalytic activity of CoFe2O4 via heterojunction formation for photocatalysis of organic pollutants in water, J. Saudi Chem. Soc. 23 (2019) 1119–1136, https://doi.org/10.1016/j.jscs.2019.07.003.

[13] J. Li, Y. Yu, L. Zhang, Bismuth oxyhalide nanomaterials: layered structures meet photocatalysis, Nanoscale 6 (2014) 8473–8488, https://doi.org/10.1039/C4NR02553A.

[14] J. Niu, P. Dai, Q. Zhang, B. Yao, X. Yu, Microwave-assisted solvothermal synthesis of novel hierarchical BiOI/rGO composites for efficient photocatalytic degardation of organic pollutants, Appl. Surf. Sci. 430 (2018) 165–175, https://doi.org/10.1016/j.apsusc.2017.07.190.

[15] S. Zou, F. Teng, C. Chang, Z. Liu, S. Wang, Controllable synthesis of uniform BiOF nanosheets and their improved photocatalytic activity by an exposed high-energy (002) facet and internal electric field, RSC Adv. 5 (2015) 88936–88942, https://doi.org/10.1039/C5RA14769G.

[16] Z. Shan, W. Wang, X. Lin, H. Ding, F. Huang, Photocatalytic degradation of organic dyes on visible-light responsive photocatalyst PbBiO2Br, J. Solid State Chem. 181 (2008) 1361–1366, https://doi.org/10.1016/j.jssc.2008.03.001.

[17] H. Huang, Y. He, Z. Lin, L. Kang, Y. Zhang, Two novel Bi-based borate photocatalysts: crystal structure, electronic structure, photoelectrochemical properties, and photocatalytic activity under simulated solar light irradiation, J. Phys. Chem. C 117 (2013) 22986–22994, https://doi.org/10.1021/jp4084184.

[18] T. Kako, Z. Zou, M. Katagiri, J. Ye, Decomposition of organic compounds over NaBiO3 under visible light irradiation, Chem. Mater. 19 (2007) 198–202, https://doi.org/10.1021/cm0611284.

[19] S.S. Dunkle, R.J. Helmich, K.S. Suslick, BiVO4 as a visible-light photocatalyst prepared by ultrasonic spray pyrolysis, J. Phys. Chem. C 113 (2009) 11980–11983, https://doi.org/10.1021/jp903757x.

[20] Z. Zou, J. Ye, H. Arakawa, Substitution effects of In3+ by Fe3+ on photocatalytic and structural properties of Bi2InNbO7 photocatalysts, J. Mol. Catal. Chem. 168 (2001) 289–297, https://doi.org/10.1016/S1381-1169(00)00545-8.

[21] J. Bi, L. Wu, J. Li, Z. Li, X. Wang, X. Fu, Simple solvothermal routes to synthesize nanocrystalline Bi2MoO6 photocatalysts with different morphologies, Acta Mater. 55 (2007) 4699–4705, https://doi.org/10.1016/j.actamat.2007.04.034.

[22] X. Zhang, Z. Ai, F. Jia, L. Zhang, Generalized one-pot synthesis, characterization, and photocatalytic activity of hierarchical BiOX (X = Cl, Br, I) nanoplate microspheres, J. Phys. Chem. C 112 (2008) 747–753, https://doi.org/10.1021/jp077471t.

[23] A. Kumar, B. Subash, B. Krishnakumar, A.J.F.N. Sobral, K.R. Sankaran, Synthesis, characterization and excellent catalytic activity of modified ZnO photocatalyst for RR 120 dye degradation under UV-A and solar light illumination, J. Water Process Eng. 13 (2016) 6–15, https://doi.org/10.1016/j.jwpe.2016.07.009.

[24] S.A. Ansari, M.M. Khan, M.O. Ansari, J. Lee, M.H. Cho, Biogenic synthesis, photocatalytic, and photoelectrochemical performance of Ag–ZnO nanocomposite, J. Phys. Chem. C 117 (2013) 27023–27030, https://doi.org/10.1021/jp410063p.

[25] M. Ebrahimi Naghani, M. Neghabi, M. Zadsar, H. Abbastabar Ahangar, Synthesis and characterization of linear/nonlinear optical properties of graphene oxide and reduced graphene oxide-based zinc oxide nanocomposite, Sci. Rep. 13 (2023) 1496, https://doi.org/10.1038/s41598-023-28307-7.

[26] T. Lv, L. Pan, X. Liu, T. Lu, G. Zhu, Z. Sun, Enhanced photocatalytic degradation of methylene blue by ZnO-reduced graphene oxide composite synthesized via microwave-assisted reaction, J. Alloys Compd. 509 (2011) 10086–10091, https://doi.org/10.1016/j.jallcom.2011.08.045.

[27] C.H. Nguyen, M.L. Tran, T.T. Van Tran, R.-S. Juang, Enhanced removal of various dyes from aqueous solutions by UV and simulated solar photocatalysis over TiO2/ZnO/rGO composites, Sep. Purif. Technol. 232 (2020) 115962, https://doi.org/10.1016/j.seppur.2019.115962.

[28] Q. Xiang, J. Yu, M. Jaroniec, Graphene-based semiconductor photocatalysts, Chem. Soc. Rev. 41 (2012) 782–796, https://doi.org/10.1039/C1CS15172J.

[29] R.J. Young, I.A. Kinloch, L. Gong, K.S. Novoselov, The mechanics of graphene nanocomposites: a review, Compos. Sci. Technol. 72 (2012) 1459–1476, https://doi.org/10.1016/j.compscitech.2012.05.005.

[30] A. V Rozhkov, G. Giavaras, Y.P. Bliokh, V. Freilikher, F. Nori, Electronic properties of mesoscopic graphene structures: charge confinement and control of spin and charge transport, Phys. Rep. 503 (2011) 77–114, https://doi.org/10.1016/j.physrep.2011.02.002.

[31] T. Lu, L. Pan, H. Li, G. Zhu, T. Lv, X. Liu, Z. Sun, T. Chen, D.H.C. Chua, Microwave-assisted synthesis of graphene–ZnO nanocomposite for electrochemical supercapacitors, J. Alloys Compd. 509 (2011) 5488–5492, https://doi.org/10.1016/j.jallcom.2011.02.136.

[32] S. Vadivel, V.P. Kamalakannan, N.P. Kavitha, T. Santhoshini Priya, N. Balasubramanian, Development of novel Ag modified BiOF squares/g-C3N4 composite for photocatalytic applications, Mater. Sci. Semicond. Process. 41 (2016) 59–66, https://doi.org/10.1016/j.mssp.2015.07.023.

[33] Md Saad, Siti Khatijah, et al., Two-dimensional, hierarchical Ag-doped TiO2 nanocatalysts: effect of the metal oxidation state on the photocatalytic properties, ACS Omega 3 (3) (2018) 2579–2587, https://doi.org/10.1021/acsomega.8b00109.

[34] Mehran Sookhakian, et al., Enhanced photovoltaic performance of polymer hybrid nanostructure heterojunction solar cells based on poly (3-hexylthiophene)/ZnS/ZnO/reduced graphene oxide shell–core nanorod arrays, Ind. Eng. Chem. Res. 53 (37) (2014) 14301–14309, https://doi.org/10.1021/ie501677r.

[35] I. Boukhoubza, et al., X-ray diffraction investigations of nanostructured ZnO coated with reduced graphene oxide, J. Phys. Conf. 1292 (2019) 1, https://doi.org/10.1088/1742-6596/1292/1/012011.

[36] Monique R. D'Oliveira, et al., In situ DRIFTS investigation of ethylene oxidation on Ag and Ag/Cu on reduced graphene oxide, Catal. Lett. 150 (2020) 3036–3048.

[37] H. Huang, X. Li, J. Wang, F. Dong, P.K. Chu, T. Zhang, Y. Zhang, Anionic group self-doping as a promising strategy: band-gap engineering and multi-functional applications of high-performance CO32−-doped Bi2O2CO3, ACS Catal. 5 (2015) 4094–4103, https://doi.org/10.1021/acscatal.5b00444.

[38] S.B. Aziz, G. Hamasalih, M. Brza, S. Jalal, R. Abdulwahid, S. Raza Saeed, A. Hassanzadeh, Fabrication of interconnected plasmonic spherical silver nanoparticles with enhanced localized surface plasmon resonance (LSPR) peaks using quince leaf extract solution, Nanomaterials 9 (2019) 1557, https://doi.org/10.3390/nano9111557. Basel, Switzerland.

[39] L. Hu, S. Dong, Q. Li, J. Feng, Y. Pi, M. Liu, J. Sun, J. Sun, Facile synthesis of BiOF/Bi2O3/reduced graphene oxide photocatalyst with highly efficient and stable natural sunlight photocatalytic performance, J. Alloys Compd. 633 (2015) 256–264, https://doi.org/10.1016/j.jallcom.2015.02.067.

[40] A. Thakur, S. Kumar, V.S. Rangra, Synthesis of reduced graphene oxide (rGO) via chemical reduction, AIP Conf. Proc. 1661 (2015) 80032, https://doi.org/10.1063/1.4915423.

[41] E.R. Morales, N.R. Mathews, D. Reyes-Coronado, C.R. Magaña, D.R. Acosta, G. Alonso-Nunez, O.S. Martinez, X. Mathew, Physical properties of the CNT:TiO2 thin films prepared by sol–gel dip coating, Sol. Energy 86 (2012) 1037–1044, https://doi.org/10.1016/j.solener.2011.06.027.

[42] W. Su, J. Wang, Y. Huang, W. Wang, L. Wu, X. Wang, P. Liu, Synthesis and catalytic performances of a novel photocatalyst BiOF, Scripta Mater. 62 (2010) 345–348, https://doi.org/10.1016/j.scriptamat.2009.10.039.

[43] S. Vadivel, B. Paul, D. Maruthamani, M. Kumaravel, T. Vijayaraghavan, S. Hariganesh, R. Pothu, Synthesis of yttrium doped BiOF/RGO composite for visible light: photocatalytic applications, Mater. Sci. Energy Technol. 2 (2019) 112–116, https://doi.org/10.1016/j.mset.2018.11.006.

[44] J. Cheng, L. Frezet, P. Bonnet, C. Wang, Preparation and photocatalytic properties of a hierarchical BiOCl/BiOF composite photocatalyst, Catal. Lett. 148 (2018) 1281–1288, https://doi.org/10.1007/s10562-018-2296-5.

[45] M. Rafatullah, O. Sulaiman, R. Hashim, A. Ahmad, Adsorption of methylene blue on low-cost adsorbents: a review, J. Hazard Mater. 177 (2010) 70–80, https://doi.org/10.1016/j.jhazmat.2009.12.047.

[46] A. Sivakumar, B. Murugesan, A. Loganathan, P. Sivakumar, A review on decolourisation of dyes by photodegradation using various bismuth catalysts, J. Taiwan Inst. Chem. Eng. 45 (2014) 2300–2306, https://doi.org/10.1016/j.jtice.2014.07.003.

[47] P. Raizada, A. Sudhaik, P. Singh, P. Shandilya, P. Thakur, H. Jung, Visible light assisted photodegradation of 2,4-dinitrophenol using Ag2CO3 loaded phosphorus and sulphur co-doped graphitic carbon nitride nanosheets in simulated wastewater, Arab. J. Chem. 13 (2020) 3196–3209, https://doi.org/10.1016/j.arabjc.2018.10.004.
[48] A.K. Dutta, S.K. Maji, B. Adhikary, γ-Fe2O3 nanoparticles: an easily recoverable effective photo-catalyst for the degradation of rose bengal and methylene blue dyes in the waste-water treatment plant, Mater. Res. Bull. 49 (2014) 28–34, https://doi.org/10.1016/j.materresbull.2013.08.024.
[49] N.M. Mahmoodi, Zinc ferrite nanoparticle as a magnetic catalyst: synthesis and dye degradation, Mater. Res. Bull. 48 (2013) 4255–4260, https://doi.org/10.1016/j.materresbull.2013.06.070.
[50] R. Qian, H. Zong, J. Schneider, G. Zhou, T. Zhao, Y. Li, J. Yang, D.W. Bahnemann, J.H. Pan, Charge carrier trapping, recombination and transfer during TiO2 photocatalysis: an overview, Catal. Today 335 (2019) 78–90, https://doi.org/10.1016/j.cattod.2018.10.053.
[51] Y. Wang, J. Li, Y. Zhou, Z. Gao, W. Zhu, L. Liu, Interfacial defect mediated charge carrier trapping and recombination dynamics in TiO2-based nanoheterojunctions, J. Alloys Compd. 872 (2021) 159592, https://doi.org/10.1016/j.jallcom.2021.159592.